Journal of Adhesion Science and Technology 23 (2009) 1215–1237

Superhydrophobic Coatings with Reduced Ice Adhesion

D. K. Sarkar ∗ and M. Farzaneh
Canada Research Chair on Atmospheric Icing Engineering of Power Networks (INGIVRE) and
Industrial Chair on Atmospheric Icing of Power Network Equipment (CIGELE), Université du
Québec à Chicoutimi (UQAC), 555 Boulevard de l'Université, Chicoutimi, Québec, G7H 2B1, Canada

DOI:10.1163/156856109X433964

Abstract
A brief description of how superhydrophobicity can help mitigate the ice accretion problem on power network equipment and other exposed structures by reducing ice-to-surface adhesion is presented. Basic models, namely the Wenzel and Cassie–Baxter models, accounting for the contact angle of water on solid surfaces relating to the influence of surface roughness on hydrophobicity are discussed. The results on superhydrophobic aluminum surfaces, superhydrophobic nanostructured silver thin films, superhydrophobic nanostructured zinc oxide as well as superhydrophobic nanofibres are also discussed. Some of the superhydrophobic surfaces were tested for ice adhesion and a reduced ice adhesion was obtained.

Keywords
Chemical etching, sol–gel, chemical bath deposition, superhydrophobic, icephobic

1. Introduction
Ice buildup on overhead transmission and distribution lines may lead to mechanical line failure or insulator flashovers, entailing both power outages and often major costs. As a matter of fact, the ice storm that hit Eastern Canada in January 1998 caused several billions of dollars in damage to the power networks (Fig. 1) and great hardship among hard-hit communities.
Over the past decades, researchers have tried to improve on the traditional — thermal, mechanical and chemical — de-icing methods currently in use. Among these, freezing-point depressants (salt, chemical sprays, etc.) for highways [1[1]] and de-icing fluids (ethylene and propylene glycols) for aircraft [2] have drawbacks as to frequency of application, cost and toxicity. Other methods, specifically applicable

[1] ∗ To whom correspondence should be addressed. Tel.: 1-418-545-5011, ext. 2543; Fax: 418-545-5012; e-mail: dsarkar@uqac.ca

Figure 1. Image of fallen wood poles due to ice deposited on metal cables.

to transmission lines, such as mechanical vibration of cables, Joule heating of the conductors [1] and electrolysis [3] are effective but consume considerable amount of energy and necessitate surveillance of the lines and on-site intervention. Moreover, none of these techniques prevents ice from forming or accumulating in the first place. Preventing ice from forming on surfaces at sub-zero temperatures may be accomplished by producing coating materials that are icephobic in nature. Therefore, understanding of the ice–solid interface should be considered an important aspect in achieving icephobic surfaces.

The strong adhesion of ice to materials is mainly a property of the ice–solid interface where polar ice molecules strongly interact with the solid. Among the three physical processes involved in ice adhesion, namely, hydrogen bonding, van der Waals forces, and direct electrostatic interactions, the last has been found to be the dominant factor [4, 5]. The electrostatic interaction energy between ice and metals is significantly higher than the chemical bonding energy and van der Waals forces [6]. Charges on ice induce equal and opposite charges on metals, whereas on dielectrics, induced charge is smaller and is related to the dielectric constant by the following equation:

$$q' = q\frac{\varepsilon - 1}{\varepsilon + 1}, \tag{1}$$

where $q\_$ is the image charge induced by a charge q on the ice surface and ε is the dielectric constant of the insulating material on which ice is deposited [6]. Therefore, the interaction force between ice and a metal is greater than that between ice and a dielectric material. Based on the above equation, materials with a very low dielectric constant would significantly reduce the adhesion of ice by reducing the electrostatic interaction.

In addition to the influence of electrostatic forces on ice adhesion, the morphology and composition of the iced solid surface plays an important role. Studies have been carried out in an attempt to understand the role of surface roughness on ice adhesion using the concept of superhydrophobicity [7, 8].

1.1. Superhydrophobicity in Nature

A surface exhibiting nearly zero wetting is said to be 'superhydrophobic'. Superhydrophobicity is observed on certain natural tissues. Among them, the surface of lotus leaves is the most obvious candidate for its inherent superhydrophobic and self-cleaning properties (Fig. 2(a)). The so-called 'Lotus effect' is due to the presence of a rough micro–nanostructure (Fig. 2(b)) covered with waxy materials with a high degree of resistance to wetting, resulting in a water contact angle slightly above 150◦ [9]. Superhydrophobicity in nature is not limited to just lotus leaves. Several other plants, animals and insects possess superhydrophobic properties.Water striders [10] can easily stand and walk on water due to the special non-wetting feature of their legs (Fig. 2(c)). The water repellency of their legs, according to Gao and Jiang [10], is due to the legs' special hierarchical structure, as they are covered with large numbers of oriented tiny hairs (microsetae) with fine nanogrooves coated with waxy materials (Fig. 2(d)). The contact angle of the insect's legs with water is greater than 160◦. Research indicates that water droplets easily roll off the surface of butterfly wings (Fig. 2(e)), a special ability resulting from the direction-dependent arrangement of flexible nano-patterns on ridging nano-stripes and micro-scales overlapped on the wings at the one-dimensional level (Fig. 2(f)), where two distinct contact modes of a droplet with orientation-tunable microstructures occur and thus produce different adhesion forces [11, 12].

The rough structure allows for large amounts of air to be trapped between the gaps of the micro/nanostructure, resulting in a heterogeneous surface composite, where air and the waxy tissue provide very low surface energy enhancing the contact angle of the rough structure. Learning from nature, superhydrophobicity can be obtained by creating a surface with optimum roughness followed by passivation with a low-surface-energy coating. As the contact area of water on a superhydrophobic solid surface is negligible, such surfaces would effectively reduce the contact area of ice as well. Therefore, ice adhesion would be significantly reduced on superhydrophobic surfaces.

1.2. Classical Models Governing Wettability

A very basic and commonly used relation (equation (2)) describing wettability with respect to the contact angle of a drop in equilibrium with a solid surface was given by Young [13]. It relates the interfacial free energies of the three interfaces the drop comes into contact with, when placed on a solid surface, namely the solid/liquid (γSL), solid/vapor (γSV) and liquid/vapor (γLV) interfaces. The line of contact with the three co-existing phases of the system makes an angle of contact, θ, with the surface, as shown in Fig. 3:

$$\cos\theta = \frac{\gamma_{SV} - \gamma_{SL}}{\gamma_{LV}}. \tag{2}$$

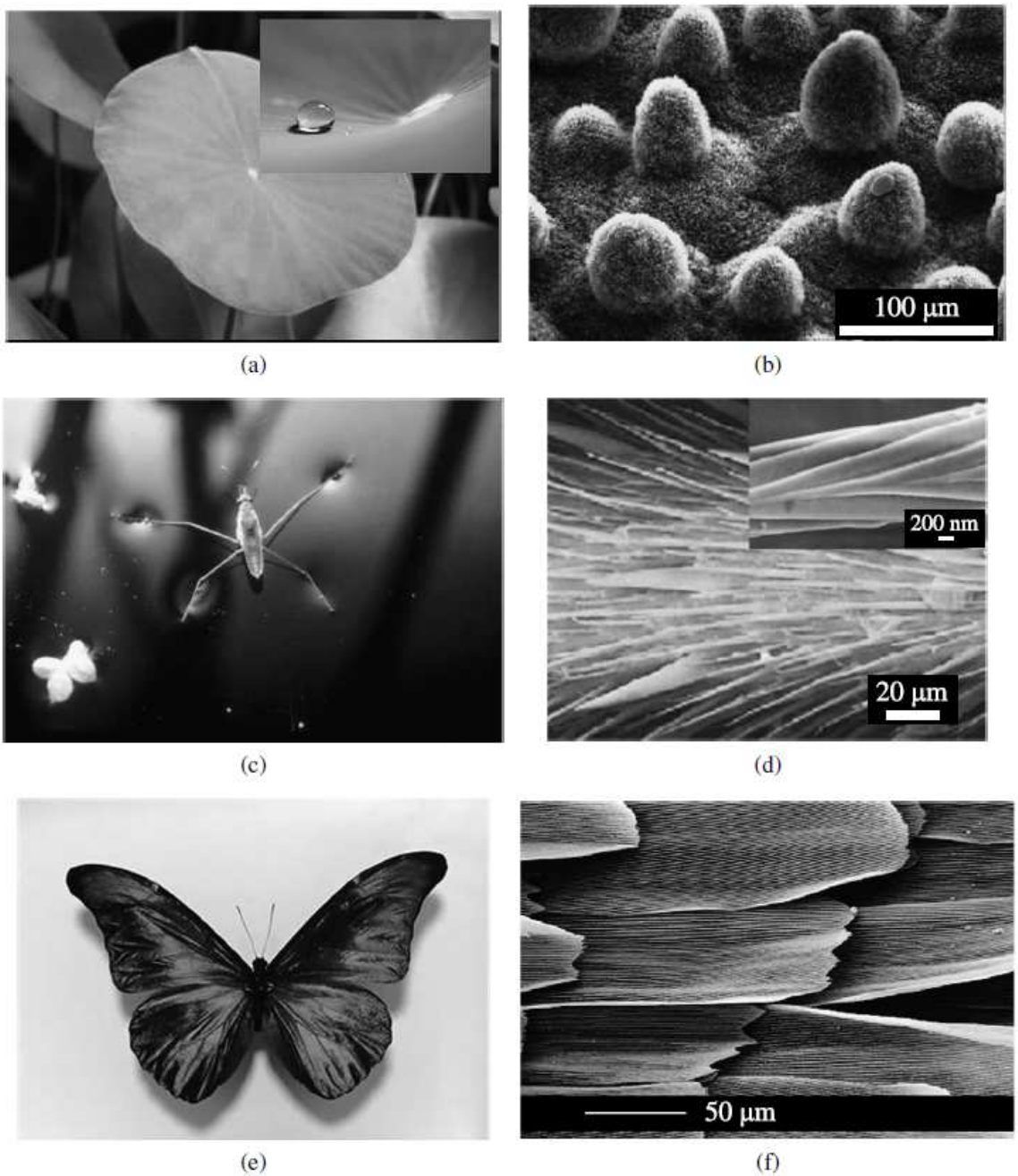

Figure 2. (a) Water drop on a lotus leaf, (b) microstructure of a lotus leaf, (c) water strider on water surface, (d) microstructure of a water strider leg showing the special hierarchical arrangement of large numbers of oriented tiny hairs (microsetae) with fine nanogrooves coated with waxy materials, (e) a colorful picture of a butterfly and (f) the microstructure of a butterfly wing.

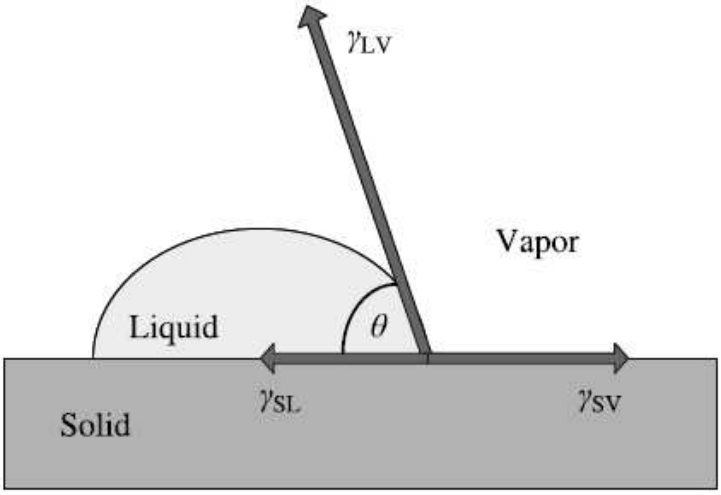

Figure 3. A water drop in equilibrium state on a surface, as presented by Young.

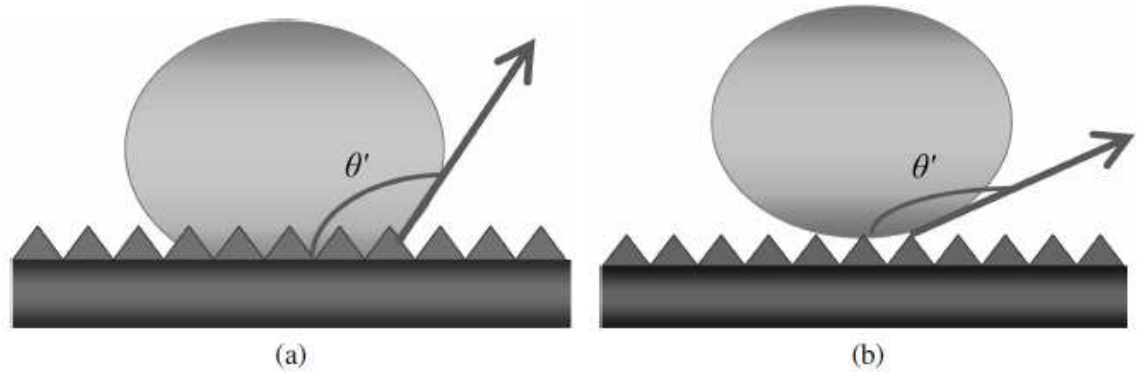

Figure 4. (a) Wenzel model and (b) Cassie–Baxter model.

To reach contact angle values greater than 150◦, necessary for achieving superhydrophobicity, surface roughness is often added to enhance the hydrophobicity of the solid surface. The surface topography effects have been mathematically expressed by the Wenzel and the Cassie–Baxter equations [14, 15]. The Wenzel equation is expressed as:

$$\cos\theta' = R_{\mathrm{w}} \cos\theta, \tag{3}$$

where the roughness factor *R*w is the ratio of the true to the apparent surface areas. Figure 4(a, b) depicts the behavior of a water drop based on Wenzel and Cassie– Baxter models.

The Cassie–Baxter model, however, describes the effect of roughness on chemically heterogeneous structures where the apparent contact angle is mathematically derived from the Cassie equation, as follows:

$$\cos\theta' = f_1 \cos\theta_1 + f_2 \cos\theta_2, \tag{4}$$

where θ _ is the contact angle of the composite surface consisting of two components with contact angles θ1 and θ2, and their corresponding area fractions f1 and f2. In such a composite system, f1 is assumed to be the area fraction of the solid surface and f2 is assumed to be that of air, where θ2 is 180◦. As f1 + f2 = 1, equation (4) can be further modified as:

$$\cos\theta' = f_1(\cos\theta_1 + 1) - 1. \quad (5)$$

This equation explains why on a rough surface with a large amount of air entrapment in the surface irregularities, one can obtain a highly superhydrophobic surface with a very small area fraction f1 of the surface in contact with the water drop.

1.3. The Contribution of Nanotechnology to Superhydrophobic Surface Engineering

Nanotechnology presents paramount advantages in that it facilitates the integration and miniaturization of devices, resulting in a variety of scientific developments including environmental safety, energy consumption, miniaturization, and many others [16–25]. Wettability is a fundamental property of solid surfaces which plays an important role in daily life and several industrial applications [26]. On the other hand, various phenomena such as contamination, snow accretion and erosion are expected to be inhibited on superhydrophobic surfaces [27]. Superhydrophobic nanostructured surfaces may also play an important role in reducing snow and ice adhesion to surfaces [8] along with anti-corrosive effects, which may lead to important applications such as coatings for cables, insulators, aircraft wings, ship hulls, glass structures, windshields, etc. The two essential factors associated with achieving superhydrophobic properties are optimized surface roughness as well as low surface energy. Inspired by surface engineering found in nature, and using the concepts provided by the Wenzel and Cassie–Baxter models, the ways for preparing superhydrophobic surfaces can be generally categorized into the 'topdown' and 'bottom-up' approaches. Top-down approaches encompass lithographic and template-based techniques [28], and plasma treatment of the surfaces [29, 30]. Bottom-up approaches involve mostly self-assembly and self-organization [31], such as chemical bath deposition (CBD) [32, 33], chemical vapor deposition (CVD) [34], and electrochemical deposition [35]. Techniques involving the combination of both approaches, such as polymer solution casting, phase separation [36] and electrospinning [37, 38], are also commonly used.

The research activities carried out in our group are unique, as compared to those of several other research groups also working in the field of superhydrophobicity, due to the fact that our facilities are designed to not only conduct superhydrophobicity tests, but ice adhesion tests on surfaces as well.

2. Experimental: Nanopartilces and Nanostructured Thin Films

2.1. Various Processes for Depositing Thin Films

2.1.1. Microemulsion Process

In this process, metallic nanoparticles are prepared from metallic salts in an alcoholic medium which acts both as solvent and reducing agent of metallic ions. For the preparation of silver nanoparticles, for example, a certain volume of ethylene glycol (EG) is heated to 160◦C under vigorous stirring in a round-bottomed, threenecked flask. Solutions of AgNO3 and poly(vinyl pyrrolidone) (PVP), both in EG, are then prepared and simultaneously injected into the flask, followed by continuous stirring to obtain silver nanoparticles.

2.1.2. Sol–Gel Technique

The sol–gel process involves the evolution of inorganic networks through the formation of a colloidal suspension (sol) and the gelation of the sol to form a network in a continuous liquid phase (gel) [38]. The precursors for synthesizing these colloids consist of a metal or metalloid element surrounded by various reactive ligands. Metal alkoxides are most used because they react readily with water. ZnO thin films were prepared on silicon, aluminum (Al) and on etched Al substrates.
The desired molar concentration of methanolic ZnO was prepared from a stock of 0.5 M methanolic ZnO prepared by dissolving 10.975 g of zinc acetate dehydrate ($Zn(CH3COO)2 \cdot 2H2O$) (Sigma Aldrich) in 100 ml of methanol under constant stirring at 500 rpm on a hotplate maintained at 80◦C. The zinc acetate dissolved in 5 min and the sol was transparent. The sol was stirred for a period of 30 min and aged for 48 h prior to spin-coating on the substrates. The 48-h aged, transparent ZnO sol was deposited drop-wise onto the substrates and spin-coated at 3000 rpm for 30 s. The spin-coated samples were dried on a hotplate at a temperature of 120◦C for 30 min and then annealed in air at 450◦C for 30 min. The annealed samples were cooled to room temperature prior to any further treatment or characterization.

2.1.3. Plasma Deposition (PECVD/PVD)
Aside from thin film deposition using chemical processes, we also utilized a plasma reactor allowing for plasma enhanced chemical vapor deposition (PECVD), as well as physical vapor deposition (PVD). In the PECVD process, hard films of diamondlike-carbon (DLC) are routinely prepared using $CH4$ and Ar gas discharges with an rf-source. In addition, low-surface-energy fluorinated DLC (F-DLC) hard coatings are produced by incorporating fluorine using $C2F6$ gas during DLC deposition. In the PVD process, a Teflon target is sputtered to produce thin films of Teflon on nanostructured surfaces to obtain low-surface-energy superhydrophobic coatings.

2.1.4. Atomic Force Microscopy (AFM)
The EnviroScope atomic force microscope combines modular environmental controls, a sealed hermetic sample chamber, and a wide range of imaging modes to bring superior application flexibility to research and industrial facilities. The system allows for observing sample reactions in a variety of complex environmental changes. The EnviroScope's scanner includes a piezoelectric tube scanner, a laser, and a quadrature optical detector capable of delivering proven scanning probe performance and reliability. The microscope is capable of imaging zero to −10◦C samples, and is suitable for the study of ice/matter interactions.

2.1.5. Drop Analysis: Contact Angle Measurement
The Drop Shape Analysis System DSA100 provided by Krüss GmbH is an ideal tool for measuring the contact angle of a drop of liquid on a surface, as well as the contact angle hysteresis. This system can be used for the evaluation of surface treatments, examine adhesion properties, check surface purity and optimize a broad range of coatings. An additional special stage has been attached that can bring the sample surface temperature to below −20◦C and make this system suitable for contact angle measurements below 0◦C.
Apart from the materials synthesis facilities, our lab is equipped with several cold chambers to produce atmospheric ice, as well as mechanical test systems (MTS) which measure ice adhesion on solid surfaces, bending strength and stress of atmospheric ice, and perform several other ice adhesion tests.

2.1.6. Ice Adhesion Test

An experimental set-up was developed at one of our cold chambers to evaluate the ice adhesion force with different materials. A thermocoal block with a hole drilled through the center is used as the mold to grow the ice. The thermocoal mold is placed at the center of the sample surface and fixed with an adhesive tape. The sample surface is placed at the bottom of the mold and distilled water is poured in. Then, an inverted screw is immersed in the water, held in place by a supporting block. The setup is then kept in the refrigerator (−20◦C) for more than 12 h for freezing. After removing the thermocoal, a pulley, connected to a spring balance, is used to detach the ice block from the surface, at −12◦C cold-room temperature. Figure 5 shows a schematic representation of the ice block formation. The adhesion force is calculated using the following equation:

$$\text{Adhesion force} = F/A, \quad (6)$$

where $F = mg$ is the applied force needed to remove the ice block and A is the surface area of the ice block in contact with the sample surface.

3. Results and Discussion: Studies on Nanostructured Superhydrophobic Coatings

Sarkar and coworkers have studied several nanostructured surfaces [16–19, 21–24, 39] and, recently, have demonstrated the superhydrophobic properties of these surfaces [40, 41]. In recent years, substantial progress has been made in the field of superhydrophobic coatings in our laboratory [33, 37, 40–51]. Some of our exciting findings in the field are described in this section.

3.1. Superhydrophobic Properties of Aluminum Surfaces Rolled sheets of aluminum alloy (AA6061) of dimensions 25 mm × 25 mm × 1.58 mm, were used as substrates. The substrates were etched with 14.8 wt% hydrochloric acid (HCl) for different times ranging from 1 to 5 min. The etched clean

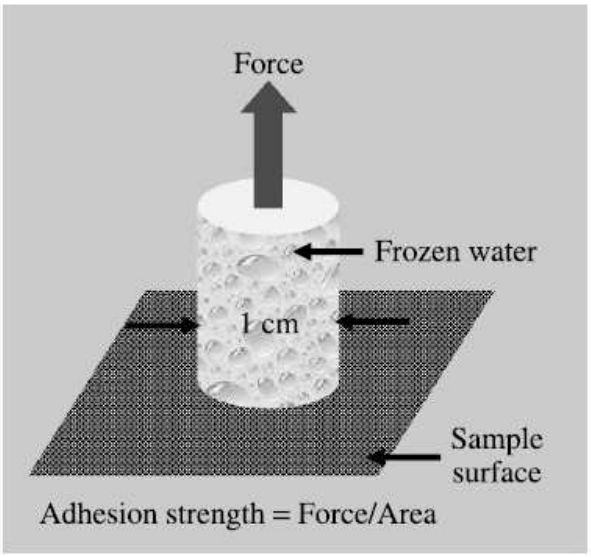

Figure 5. Schematic of the ice block formation on the sample surface.

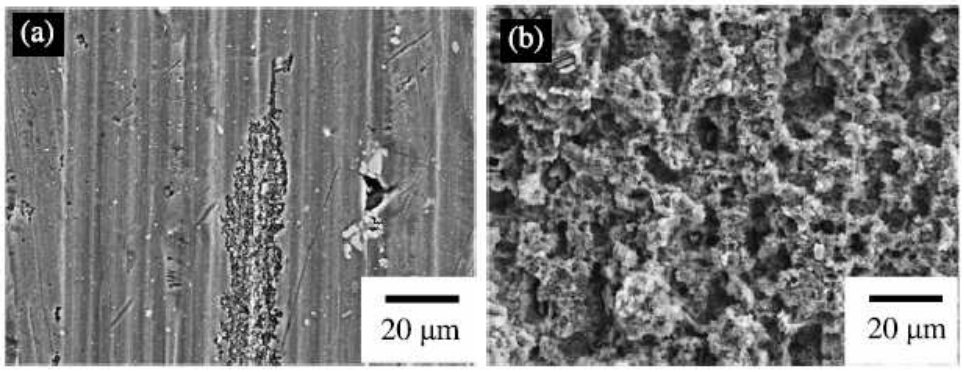

Figure 6. FESEM images of rf-sputtered Teflon-coated (a) as-received aluminum substrate and (b) aluminum substrates etched with 14.8 wt% HCl for 2.5 min.

samples were dried and further coated with ultrathin Teflon films by rf-sputtering using Ar plasma in an inductively coupled plasma reactor.

Figure 6 shows FESEM images of rf-sputtered Teflon-coated (a) as-received aluminum substrate and (b) aluminum substrates etched with 14.8 wt% HCl for 2.5 min. It is clear from Fig. 6(b) that etch pits are formed on the aluminum surface after etching with HCl acid, which effectively modifies the surface morphology [52, 53]. X-ray photoelectron spectroscopy (XPS) analysis confirms the presence and chemical composition of the rf-sputtered Teflon films. Figure 7 shows the C1s spectrum of an rf-sputtered Teflon film. Figure 8(a) shows changes in thickness of the aluminum substrates in relation to etching time. The as-received aluminum substrates are 1.58±0.006-mm thick. However, after 2.5 min of etching, the thickness is reduced to 1.46±0.014 mm, and then further reduced to 1.25±0.012 mm when etching is prolonged to 5 min.

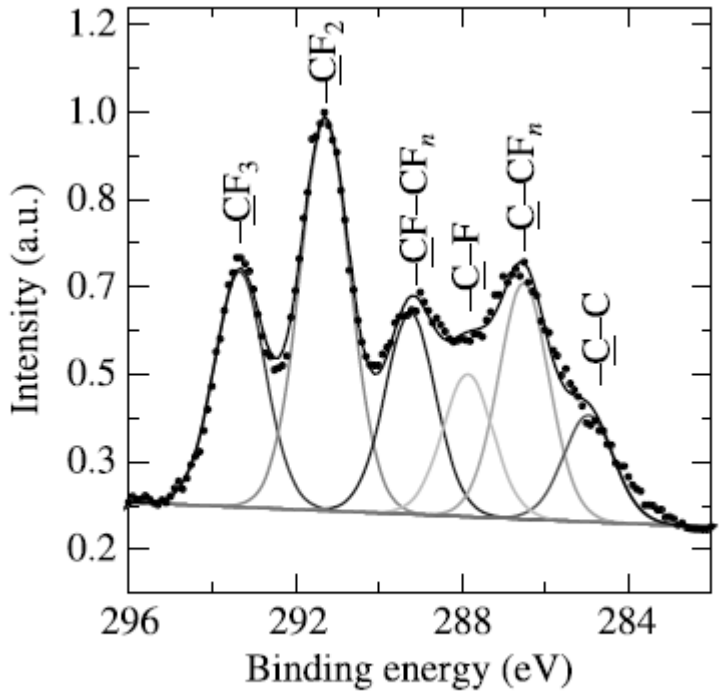

Figure 7. C_{1s} XPS spectrum of an rf-sputtered Teflon film.

The change in thickness of the aluminum substrates, etched between 2 and 5 min, follows a first-order exponential decay law with time as presented in equation (7):

$$d = 1.22 + 1.74 \exp(-t/1.28), \quad (7)$$

where *d* is the thickness of the aluminum substrates and *t* is the etching time. Figure 8(b) shows the contact angle data of water on etched aluminum substrates thinly coated with rf-sputtered Teflon. As-received aluminum substrates coated with rf-sputtered Teflon showed a contact angle of ~121 ± 1.3◦. The contact angle increased to 164 ±3◦ for the aluminum substrates that were etched for 2.5 min.
It is interesting to note that the contact angle remains constant on the aluminum surfaces that were etched for longer than 2.5 min, as shown in Fig. 8(b).
An average contact angle hysteresis of 2.5 ± 1.5◦ has been achieved on Tefloncoated etched aluminum surfaces, as shown in Fig. 8(c). The contact angle values similar to our observations or even higher have been reported in recent literature [32]. The insets of Fig. 8(b) show the shapes of water drops on 1-min and 2.5-min etched surfaces, to illustrate contact angle values. The existence of a large number of CF3 groups along with CF2 groups makes the etched aluminum surfaces highly superhydrophobic, providing a water contact angle of ~164 ± 3◦ with a very low contact angle hysteresis below 2.5±1.5◦.Water drops simply roll off such surfaces.
This simple, low-cost and efficient way of preparing substrates with superhydrophobic properties has promising industrial applications.

3.2. Superhydrophobic Properties of Silver Nanoparticles-Coated Copper Surfaces
Ultrasonically cleaned copper substrates were coated with silver thin films by immersion in a silver nitrate solution, which involves a chemical reaction in which

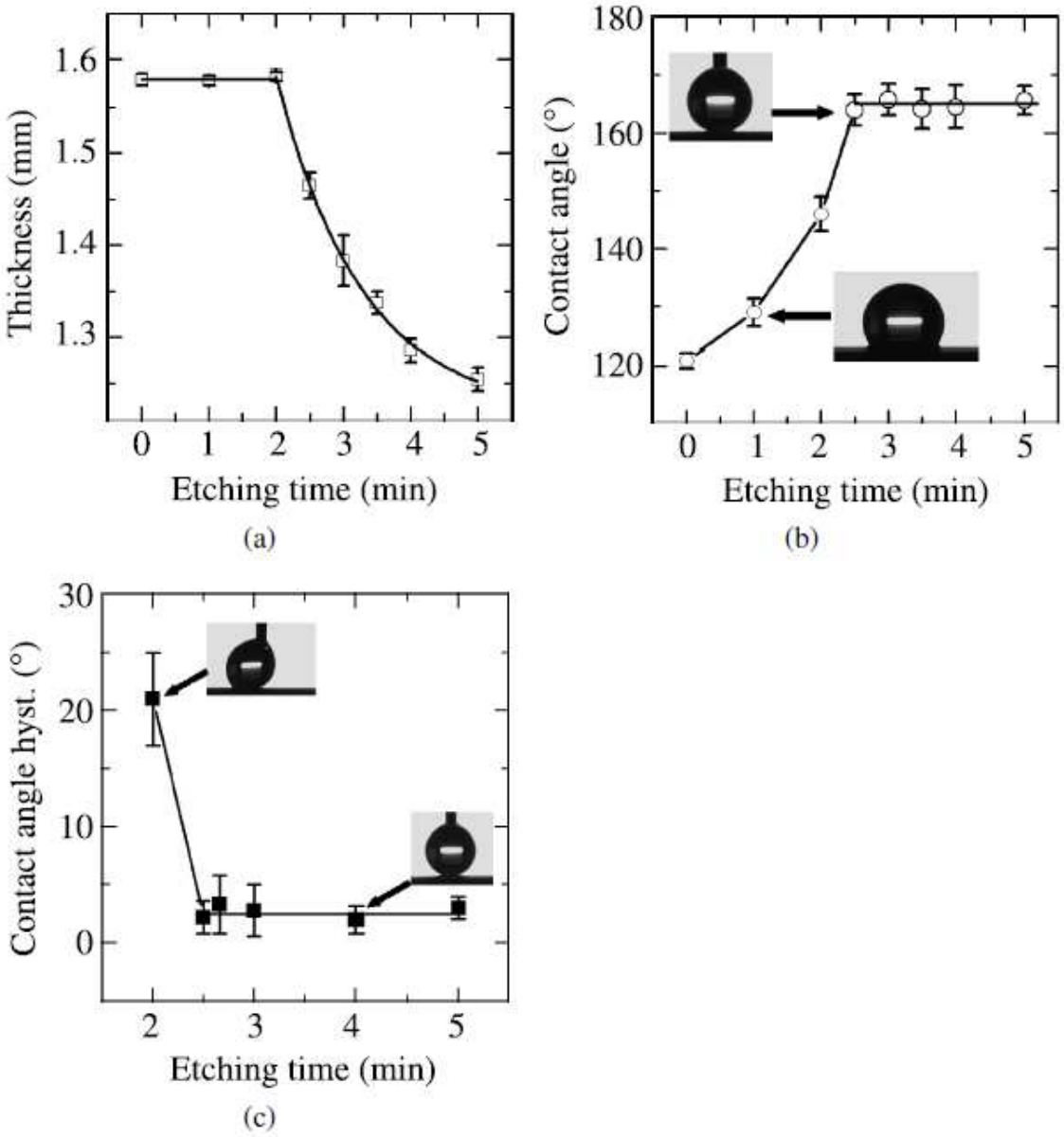

Figure 8. (a) Change in thickness of aluminum substrates with etching time, (b) contact angle of water and (c) contact angle hysteresis of water on rf-sputtered Teflon-coated aluminum substrates with different etching times. copper reduces silver ions spontaneously, as described by the following equation:

$$2Ag^{+} + Cu \rightarrow 2Ag + Cu^{2+}. \quad (8)$$

After drying, the silver-coated samples were passivated with stearic acid organic molecules dissolved in acetone. Figure 9(a–c) shows SEM images of samples prepared in three different initial Ag+ concentrations of 13.2, 24.75 and 396 mM, respectively, in the solution. It can be seen that the size and number of both the fractallike structures and voids surrounded by these fractals are concentration dependent. Due to the low Ag+ ion concentration in the solution, the reaction is slow and the film has tiny, almost indistinguishable voids, as shown in Fig. 9(a).

After stearic acid passivation, this sample shows a water contact angle and a contact angle hysteresis of 137◦ and 27◦, respectively, as shown in the inset of

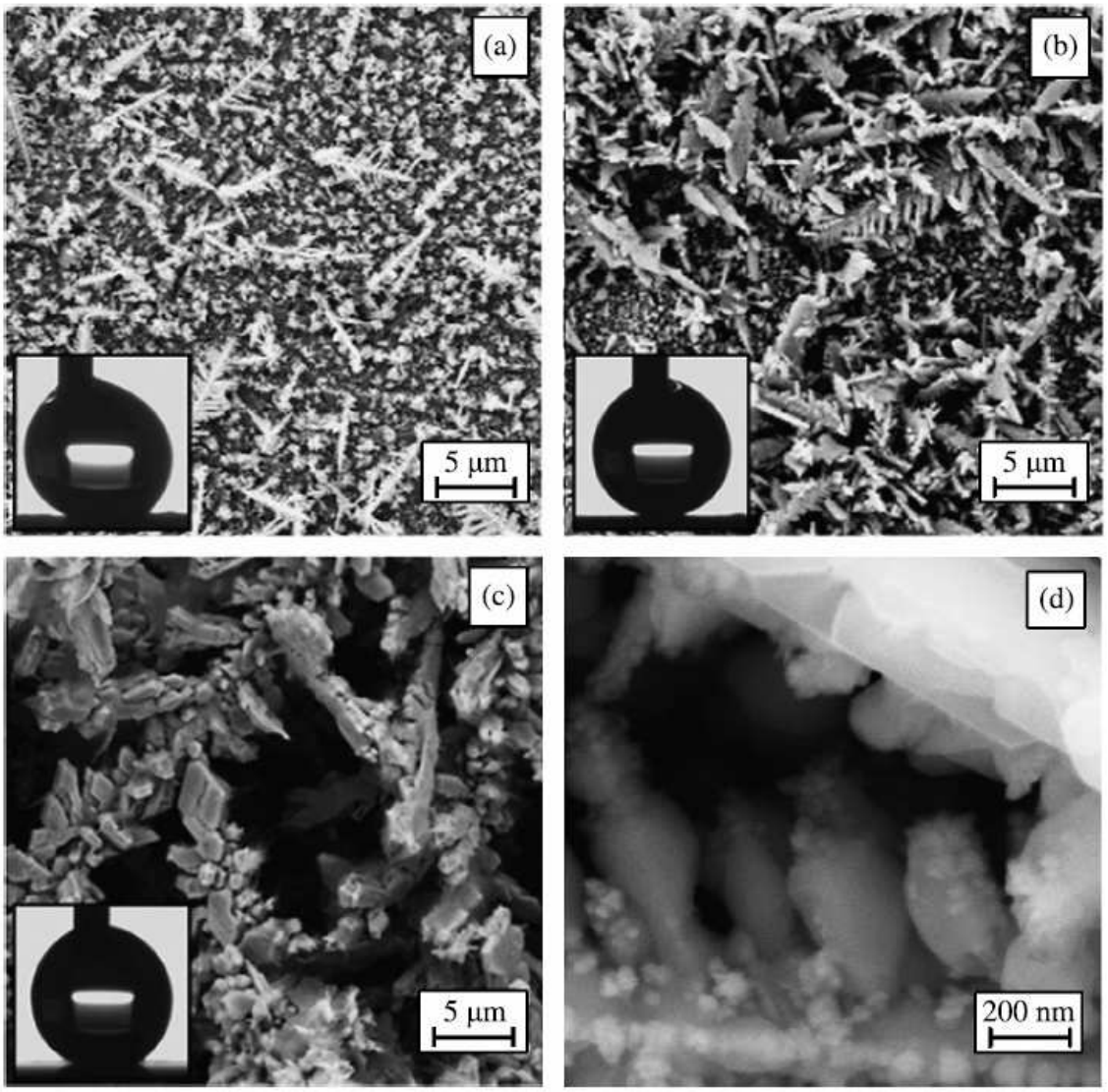

Figure 9. SEM images of samples prepared in three different initial Ag^{+} concentrations of (a) 13.2 mM, (b) 24.75 mM, (c) 396 mM and (d) a magnified section of (b).

Fig. 9(a).When the initial Ag+ ion concentration increases in the solution, reaction time increases and larger fractal-like structures of silver appear. Consequently, the size of the voids between these structures also increases. The average diameter of the voids is ∼5 µm, as shown in Fig. 9(b). The contact angle and contact angle hysteresis obtained are 156◦ and 4◦, respectively, as shown in the inset of Fig. 9(b). By further increasing the concentration of Ag+ ions in the solution, void size increases to ∼10 µm, as seen in Fig. 9(c), with a contact angle and hysteresis of 141◦ and 16◦ respectively, as shown in the inset of Fig. 9(c). The highest contact angle and the lowest contact angle hysteresis were achieved for the sample having a void size of ∼5 µm, obtained with

initial silver ion concentration of 24.75 mM in the solution. Figure 9(d) shows a magnified fractal-like structure from Fig. 9(b). It is

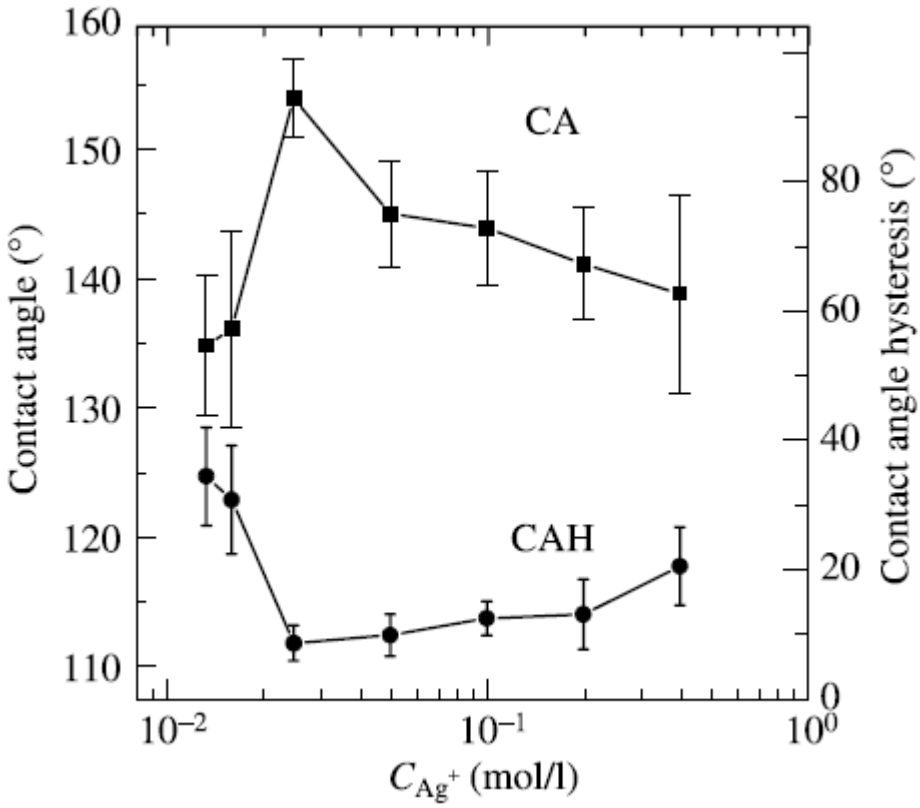

Figure 10. The variation of contact angle and contact angle hysteresis with varying silver ion concentration.

observed that aside from voids between the fractal-like structures, there are several empty spaces between them, due to its self-similar structure. Figure 10 shows the contact angle and its hysteresis for samples prepared within a given range of silver ion concentrations. The contact angle increases with the increase of silver ion concentration in the solution and reaches its maximum at 24.75 mM. Likewise, contact angle hysteresis decreases with the increase of silver ion concentration and reaches its minimum at 24.75 mM. The contact angle decreases and contact angle hysteresis increases with the further increase of silver ion concentration in the solution. In our experiment, both the highest contact angle and the lowest contact angle hysteresis were achieved with the critical solution concentration of Ag ions of ∼24.75 mM. In the experiment byWang *et al.* [54], the best hydrophobicity was achieved by HAuCl4 reagent with concentration equal to 25 mM. Comparing their experiment with ours, there is not only qualitative similarity in the morphology of fractal-like nanostructures, but also quantitative similarity in initial reagent concentrations (24.75 mM AgNO3 *versus* 25 mM HAuCl4), as well as in calculated solid fractions (0.07 and 0.096) in contact with water drop.

3.3. Superhydrophobic Properties of Nanostructured ZnO Thin Films ZnO nanotowers were grown on ultrasonically cleaned silicon substrates using the chemical bath deposition (CBD) technique, and then were dried for several hours [42]. The as-prepared ZnO samples were then passivated by 30-min immersion in 2 mM stearic acid (SA) in

acetone. Another set of sol–gel ZnO thin films spincoated using 0.02 M methanolic zinc acetate and annealing at 450◦C after drying

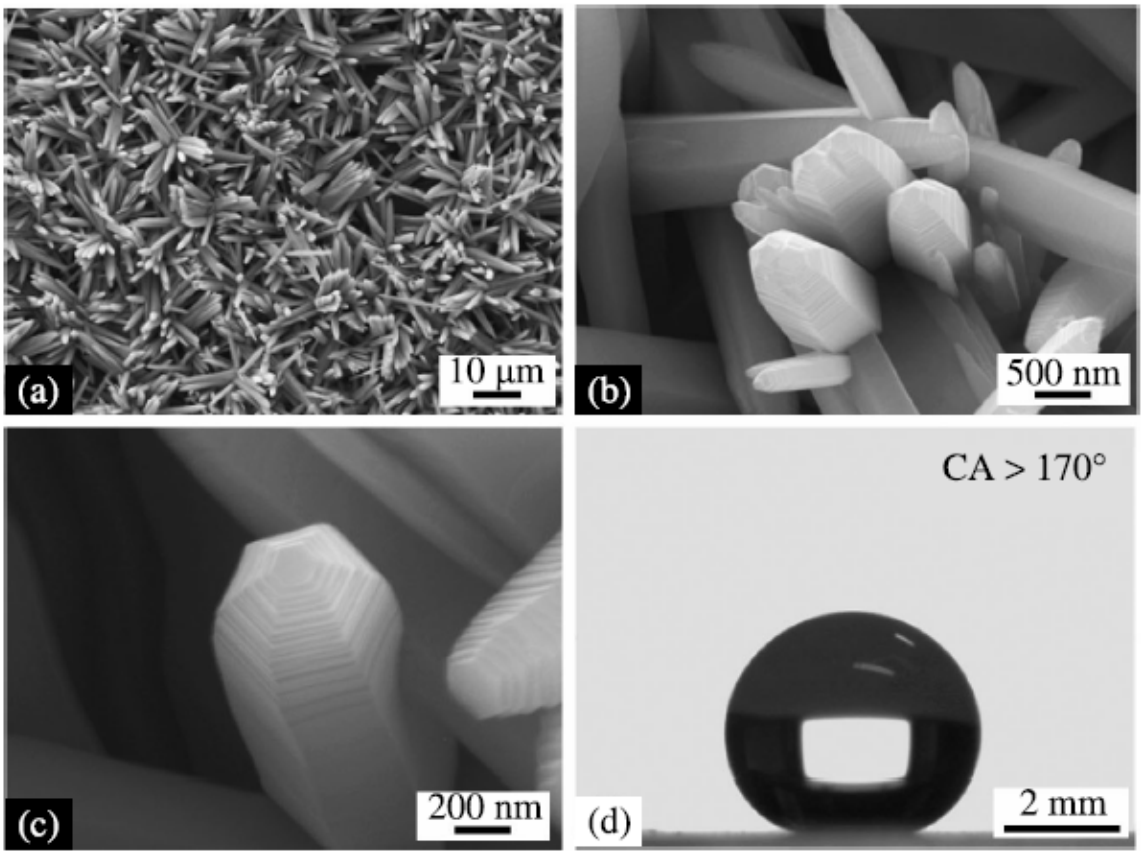

Figure 11. FESEM images of ZnO nanotowers at (a) low magnification, (b) high magnification showing the hexagonal morphology, (c) close-up view of a single nanotower showing the nanosteps and (d) image of a water drop following SA passivation.

at 120◦C on a hot plate were also passivated with 2 mM SA molecules using a method a similar to that used for CBD films. The passivated CBD grown samples were annealed in air for 30 min at temperatures ranging from 70◦C to 350◦C, for thermal desorption studies.

The growth process of ZnO nanotowers involves a chemical reaction by which the zinc nitrate decomposes to release ZnO in the presence of ammonium hydroxide [42]. Figure 11 shows the field emission scanning electron microscopy (FESEM) images of the ZnO nanotowers. While Fig. 11(a) shows the presence of randomly oriented hexagonal patterned ZnO nanotowers, characterized by regular edges with an angle of 120◦ between the adjacent sides, as shown in Fig. 11(b, c). The top few nanometers of each nanotower consist of uniform nanosteps revealing the presence of a rough binary structure.

After passivation with SA, these ZnO nanotowers become highly superhydrophobic, providing contact angles as high as ∼173◦ and contact angle hystereses as low as ∼1.5◦. However, SA passivated smooth ZnO coatings prepared by spincoating yield a contact angle of ∼73.5 ± 4◦, as shown in the inset of the AFM image of Fig. 12. To the

best of our knowledge, no such results on contact angle of water on stearic acid passivated smooth ZnO surfaces are found in the literature.
The smooth and dense sol–gel-derived spin-coated ZnO thin film is composed of scattered ~20 nm tiny ZnO particles with an *rms* roughness of ~2 nm. The con-

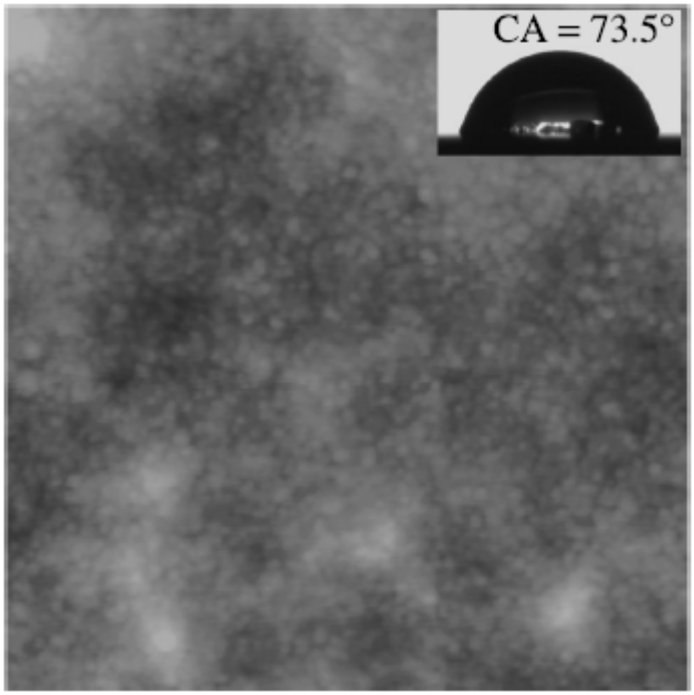

Figure 12. AFM image of spin-coated ZnO thin film with an image scan size of 1 μm × 1 μm. The inset shows the image of a water drop on this surface.

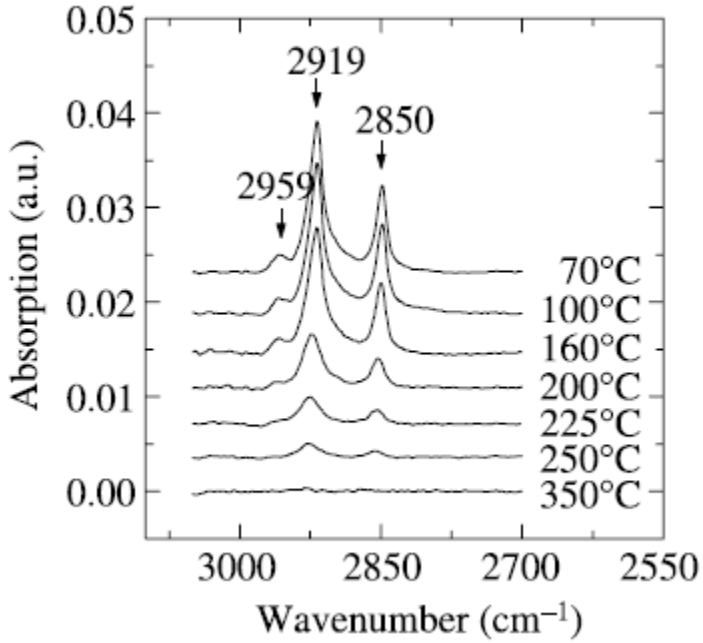

Figure 13. FT-IR spectra showing –CH*n* peaks of stearic acid following annealing at various temperatures.

tact angle results obtained are consistent with previous observations on stearic acid impregnated cellulose surface [55]. The solid surface fraction ($f1$) is calculated using the modified Cassie equation (equation (5)) for SA passivated ZnO nanotowers (composite of SA/ZnO and air) with $\theta 1$ and θ _ values of 73◦ and 173◦, respectively; and the calculated $f1$ factor is ∼0.006. Such a small value of $f1$ confirms the existence of trapped air between the nanotowers. Figure 11(d) shows the image of a water drop captured on the surface of these ZnO nanotowers after SA passivation. Fourier transform infrared (FT-IR) spectra of the SA modified ZnO nanotowers confirms the presence of the –CH*n* groups of SA. Figure 13 shows the FT-IR spec tra of the samples, annealed at different temperatures, in the wavenumber range of 2550–3150 cm−1, showing only the –CH*n* peaks of stearic acid. The two peaks at wavenumbers 2919 cm−1 and 2850 cm−1 belong to the asymmetric and symmetric C–H stretching modes of the –CH2 groups of the stearic acid respectively, and the peak at 2958 cm−1 is ascribed to the asymmetric in-plane C–H stretching mode of the –CH3 group [56]. The three peaks of stearic acid remain nearly unchanged until 160◦C, with a drastic change occurring in their intensity at 200◦C, due to thermal desorption and a continued decrease in intensity with further increase in temperature.

Figure 14 shows the contact angle and contact angle hysteresis data following annealing at elevated temperatures. The contact angle, as shown in the inset of Fig. 14, remains higher than 170◦ up to 160◦C, and then decreases slightly up to 250◦C, at which point the contact angle is greater than 160◦ and still shows superhydrophobicity. The contact angle hysteresis (Fig. 14) undergoes an increase with increasing annealing temperature, from 1.5◦ at 70◦C to 6◦ at 250◦C, although water drops still keep rolling off the surface easily. However, the contact angle continues to fall with increasing annealing temperature.

A strong correlation has been established between the thermal desorption of stearic acid and the superhydrophobic behavior of ZnO nanotowers. Figure 14 shows a nearly constant contact angle with a very low contact angle hysteresis at room temperature, following annealing at 160◦C. This is due to the presence of nearly constant stearic acid peak intensity until the annealing temperature of 160◦C is reached, as observed in Fig. 13. As the density of the stearic acid peak starts to decrease, above 160◦C, the contact angle begins to decrease, with an increase, although not great, in contact angle hysteresis. Following annealing at 350◦C, the water drop spreads completely on the surface and the FT-IR spectrum shows zero intensity –CH*n* peaks. Due to complete desorption of SA at 350◦C, the water drop

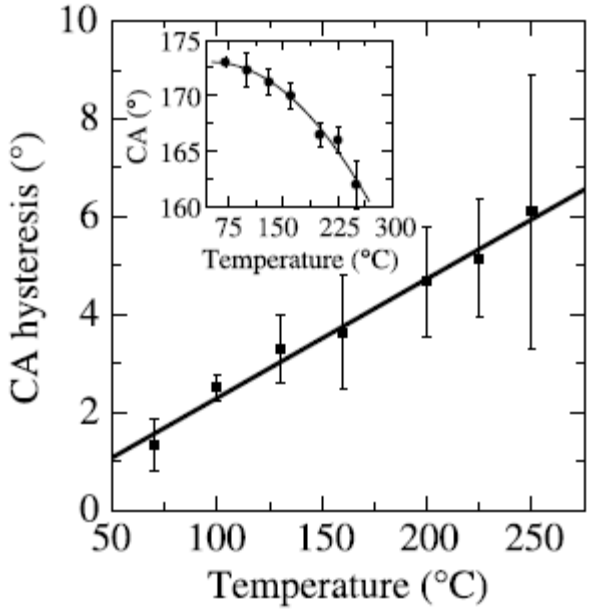

Figure 14. Contact angle hysteresis *vs* annealing temperature. Inset shows contact angle *vs* annealing temperature.

directly interacts with the ZnO, showing hydrophilic behavior of the ZnO surface.
The thermal desorption of stearic acid is found to occur at approximately 184◦C, with an activation energy of 0.34 ±0.05 eV.

3.4. Superhydrophobic Polymer Nanofibers
Polymer (polystyrene) nanofibers around 500 nm and 2 μm in diameter, for low and high viscous polymer solutions, respectively, were created by electrospinning, as shown in Fig. 15 [37]. Highly viscous solutions produced ribbon-like structures, whereas less viscous ones produced agglomerated polymer nanofibers. These polymer nanofibres do not show superhydrophobicity. To obtain superhydrophobicity, however, PTFE particles were suspended in the poly[tetrafluoroethylene-*co*- (vinylidene fluoride)-*co*-propylene] (PTVFP) polymer solution and electronspun on solid surfaces.
High-viscosity solutions yielded a fiber structure, as shown in Fig. 16(a), while the low-viscosity solutions yielded a fiber-bead-like structure with beads having an

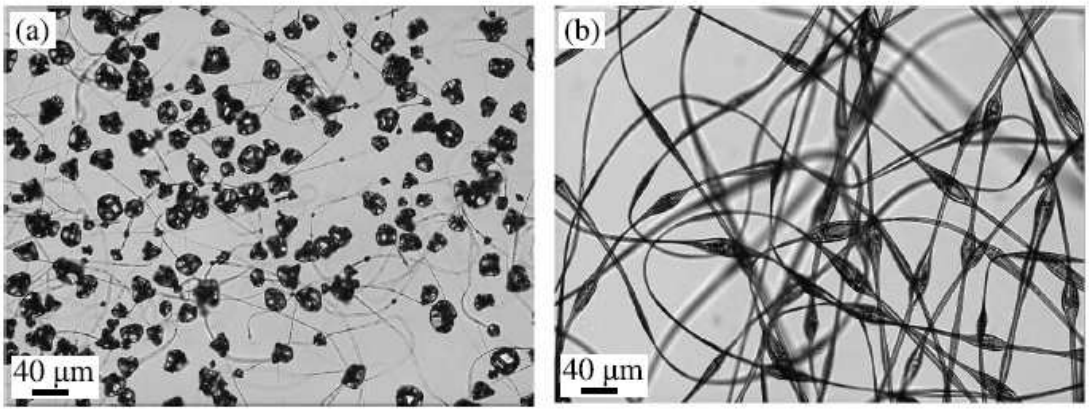

Figure 15. Optical microscopy photographs of electrospun PS mats obtained from liquid solutions with PS concentration (C_{PS}) of 14 w% (a) and 18 w% (b). (Voltage = 20 kV and flow rate = 1 ml/h.)

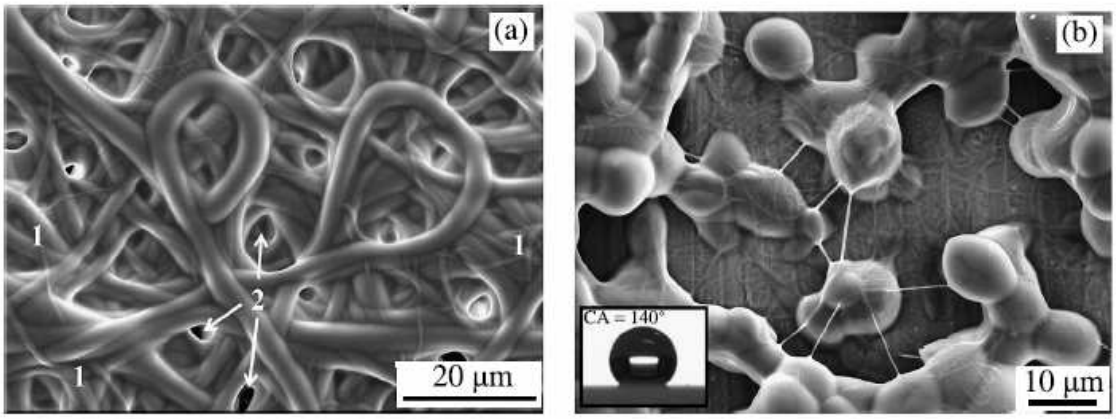

Figure 16. SEM micrographs of electrospun PTVFP mats obtained from liquid solutions with viscosity (a) 2062 mPa s and (b) 67 mPa s. (Voltage = 25 kV and flow rate = 1 ml/h.)

ellipsoidal shape (Fig. 16(b)). It is important to note that the fiber structure shown in Fig. 16(a) has closed porosity, while open porosity occurrences are scarce (see areas 1 and 2 of Fig. 16(a)). Additionally, and independently of applied voltage, increasing solution flow rates led to an increase in fiber diameters reaching as high as 9 μm. Concerning the low-viscosity solutions, the corresponding mats were made of ellipsoidal beads.

4. Influence of Superhydrophobicity on Anti-icing Properties

It has been observed that fluorinated and polysiloxane modified surfaces show the lowest water wettability and the best potential as icephobic coatings [57]. Studies have also shown that aluminum surfaces rendered hydrophobic by the addition of a self-assembled monolayer (SAM) of silane or fluorocarbon have lower ice adhesion than bare aluminum surfaces [58, 59]. It has also been reported that snow accumulation on nanostructured superhydrophobic surfaces is reduced, compared to smooth surfaces [7, 8].

4.1. Surface Compositional Analysis by XPS Before and After Ice Adhesion Testing

XPS spectra of the rf-sputtered Teflon coated dielectrics before and after ice adhesion tests are presented here in order to compare the surface composition and to determine

any loss of rf-sputtered Teflon following ice tests. Figure 17(a) shows the survey spectra and Fig. 17(b) and 17(c) show the high resolution C1s and F1s spectra, respectively of rf-sputtered Teflon-coated ZnO on etched Al prior to and after ice tests. The survey spectra before and after ice tests show strong peaks of carbon and fluorine, as expected from Teflon. These spectra are very similar as they show no significant differences in the signals of the different elements, as evident from Table 1, showing the apparent composition of the surface before and after ice tests. The F/C ratio of 1.80 on the superhydrophobic surface remains nearly the same following ice tests on the same surface, with an F/C ratio of 1.87. C1s peaks before and after ice tests do not resolve equally, as seen in Fig. 17(b). In the high-resolution F1s spectrum shown in Fig. 17(c), the F1s binding energy was found to be 688.5 eV before as well as after ice tests, with FWHM values of 2.39 eV and 2.54 eV, before and after ice tests respectively.
The broadening observed in the high-resolution C1s and F1s spectra may be due to an instrumental effect related to the neutralization of accumulated charge on the sample surface.

4.2. Ice Adhesion

Figure 18 shows the cylindrical ice block formation from frozen water using a thermocoal mold on sample surfaces, as described in the Experimental Section and depicted schematically in Fig. 5. The ice block, following separation of the thermocoal mold, just slides off the superhydrophobic surfaces, showing low ice adhesion

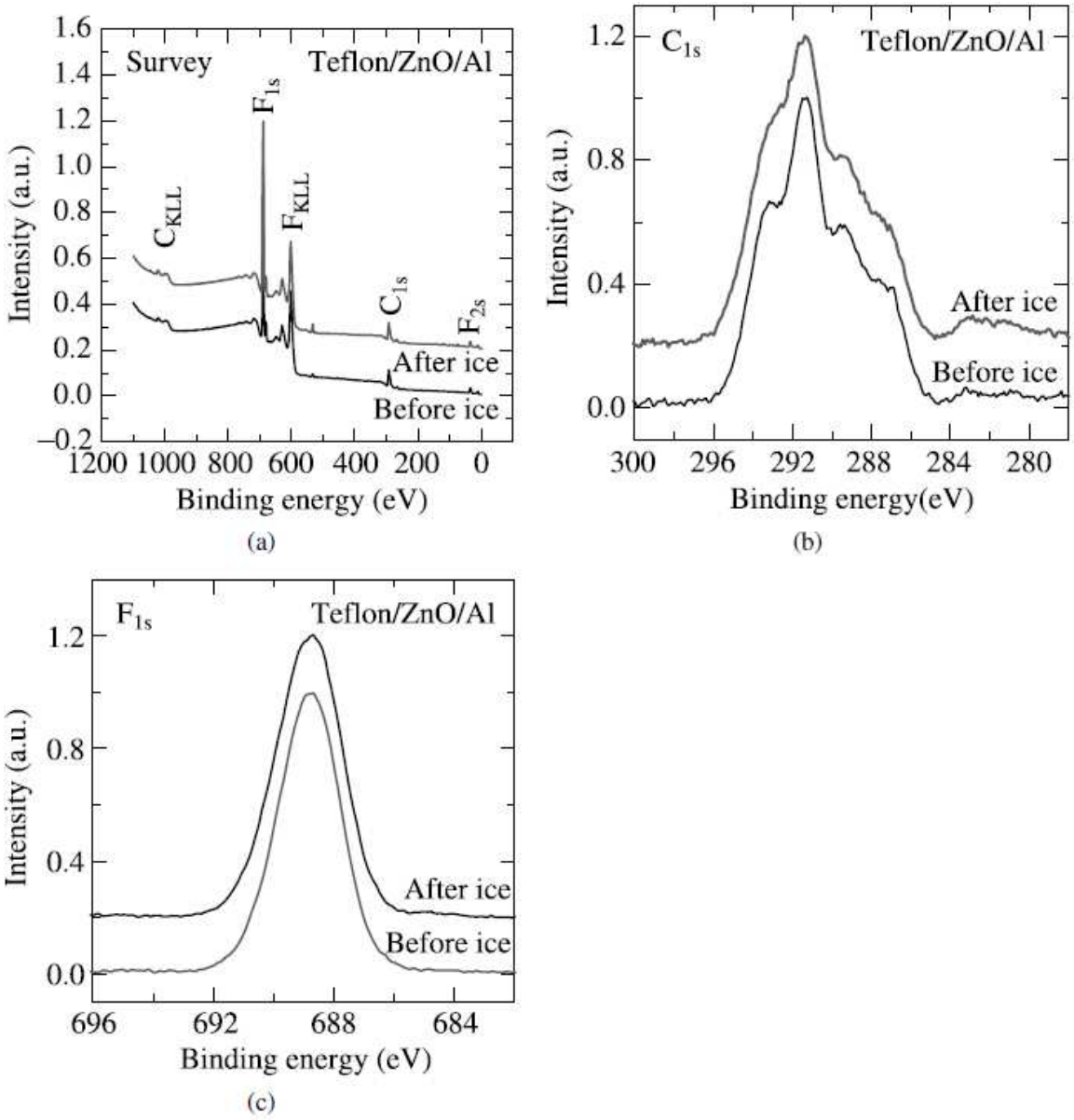

Figure 17. (a) XPS survey spectra, (b) high-resolution C1s spectra and (c) high-resolution F1s spectra of rf-sputtered Teflon-coated ZnO-coated etched Al.

Table 1.
Chemical composition of surfaces by XPS analysis before and after ice tests on rf-sputtered Teflon-coated superhydrophobic substrates

Elements	Surface chemical composition (at %)	
	Before ice tests	After ice adhesion tests
C	35	33
F	63	62
O	1.6	4

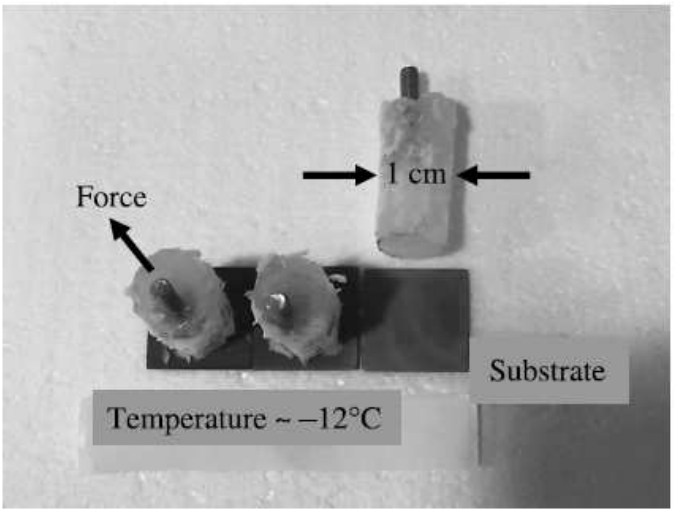

Figure 18. Photograph of cylindrical water–ice blocks frozen onto sample surfaces.

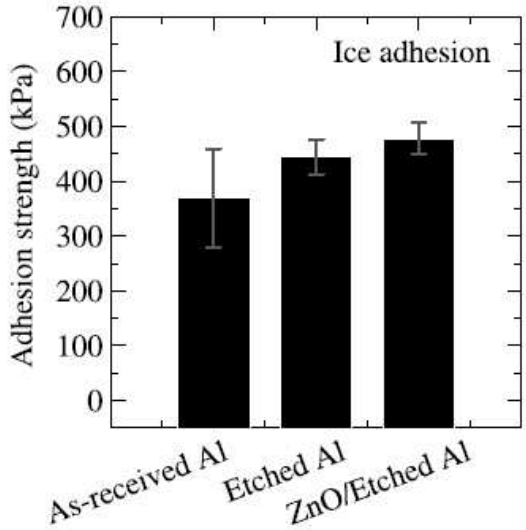

Figure 19. Ice adhesion strength on as-received Al, un-coated and dielectric thin film (ZnO) coated on etched Al surfaces.

to these surfaces; however, on the hydrophilic surfaces, the ice block is well adhered, as seen in Fig. 18. Figure 19 and Table 2 show the results of ice adhesion tests on as-received aluminum (Al), as a reference, Etched Al, and ZnO/Etched Al. The ZnO films were coated by sol–gel process to evaluate the role of dielectric thin films in ice adhesion by reducing the electrostatic force, as predicted by theory [4, 5]. The adhesion strength of ice on bare Al is found to be 369 ± 89 kPa. This value is supported by a similar value (345 ± 7 kPa) of ice adhesion strength determined by mechanical vibration on aluminum surfaces, as recently reported from our group [60].

The ice adhesion strengths on etched Al and ZnO-coated etched Al are found to be 444 ± 32 and 478 ± 28 kPa, respectively. These numbers are very similar

Table 2.
Ice adhesion strengths on hydrophilic and superhydrophobic surfaces

Samples	Ice adhesion strength (kPa)	Contact angle (°)	Contact angle hysteresis (°)
As-recieved Al	369 ± 89	74 ± 1	***
Etched Al	444 ± 32	Absorbed	***
ZnO/Etched Al	478 ± 28	Absorbed	***

*** These data could not be obtained.

when considering the error in the measurements. Hence, these experiments do not seem to explain the role of dielectric thin films in ice adhesion, as expected from theory [4, 5]. The strong ice adhesion on these surfaces is due to their hydrophilic properties, as shown in Table 2. Stronger ice adhesion on these surfaces could be due to the mechanical interlocking of ice in the pores of their rough structure, leading to complete absorption of water drops, as demonstrated by the contact angle investigation. Further work is in progress to determine ice adhesion strength more precisely by forming the ice using an ultra-low temperature (−15◦C) wind tunnel with micrometer-size water drops gusting onto the samples. These future experiments could determine the role of dielectric thin films in ice adhesion, as predicted by the theory [4, 5].

5. Summary and Conclusions

In this paper, a brief description of the problem of icing in our daily life has been described, followed by an introduction to find a probable solution to icing *via* superhydrophobicity. Several natural superhydrophobic surfaces and their microstructure were also described, along with Wenzel and Cassie–Baxter models to explain the behavior of water drops on solid surfaces and the effect of surface roughness on the enhancement of contact angle. Several interesting results were achieved on the superhydrophobicity of metals, oxides and polymers in our laboratory. Superhydrophobic micro-patterned aluminum surfaces were created by chemical etching. A water contact angle as high as 164±3◦ with a contact angle hysteresis as low as 2.5±1.5◦ were achieved on rf-sputtered Teflon-coated etched aluminum substrates. Also, a simple process was developed to produce stable superhydrophobic surfaces with contact angles as high as ∼156◦ and contact angle hystereses as low as ∼4◦, by a combination of the galvanic ion exchange reaction between silver ions and copper surfaces, and passivation with stearic acid organic molecules. As far as the superhydrophobic oxide nanostructure is concerned, it was demonstrated that stearic acid passivated ZnO nanotowers, with a binary structure composed of several nanosteps on each nanotower, have a very high contact angle of ∼173◦ with a very low contact angle hysteresis of ∼1.5◦. The ice adhesion tests have been carried out on a few superhydrophobic surfaces created on aluminum surfaces and as-received bare aluminum surfaces. The ice grown on as-received aluminum surfaces shows an adhesion strength of 369 ± 89 kPa, whereas ice spontaneously debonded from the superhydrophobic surfaces.

Acknowledgements
This study was carried out within the framework of the NSERC/Hydro-Québec/ UQAC Industrial Chair on Atmospheric Icing of Power Network Equipment (CIGELE), as well as the Canada Research Chair on the Engineering of Power Network Atmospheric Icing (INGIVRE). The authors would like to thank all the sponsors for their financial support, and are grateful to Dr R. Menini, senior researcher, to N. Saleema and A. Safaee, PhD students, and Prof. R. W. Paynter for their involvement in some tests and useful discussions.

References

1. 'Minimizing Effects from Highway Deicing', EPA 832-F-99-016 (1999).
2. 'Airplane Deicing Fluid Recovery Systems', EPA 832-F-99-043 (1999).
3. V. F. Petrenko and S. Qi, *J. Appl. Phys.* **86**, 5450 (1999).
4. S. Peng and V. F. Petrenko, *Can. J. Phys.* **81**, 387 (2003).
5. V. F. Petrenko and R. W. Whitworth, *Physics of Ice*. Oxford University Press, Oxford (1999).
6. I. A. Ryzhkin and V. F. Petrenko, *J. Phys. Chem. B* **101**, 6267 (1997).
7. C. Laforte, J.-L. Laforte and J.-C. Carrier, in: *Proceedings of the International Workshop on Atmospheric Icing of Structures (IWAIS)*, Bruno, Czech Republic, p. 6 (2002).
8. H. Saito, K. Takai and G. Yamauchi, *Surf. Coatings Int.* **80**, 4 (1997).
9. W. Barthlott and C. Neinhuis, *Planta* **202**, 1 (1997).
10. X. Gao and L. Jiang, *Nature* **432**, 36 (2004).
11. Y. Zheng, X. Gao and L. Jiang, *Soft Matter* **3**, 178 (2007).
12. J. Huang, X. Wang and Z. L. Wang, *Nano Lett.* **6**, 2325 (2006).
13. T. Young, *Phil. Trans. R. Soc. Lond.* **95**, 65 (1805).
14. R. N. Wenzel, *Ind. Eng. Chem.* **28**, 988 (1936).
15. A. B. D. Cassie and S. Baxter, *Trans. Faraday Soc.* **40**, 546 (1944).
16. D. K. Sarkar, D. Brassard and M. A. El Khakani, *Appl. Phys. Lett.* **87**, 253180 (2005).
17. D. K. Sarkar, F. Cloutier and M. A. El Khakani, *J. Appl. Phys.* **97**, 084302 (2005).
18. D. K. Sarkar, D. Brassard, M. A. El Khakani and L. Ouellet, *Thin Solid Films* **515**, 4788 (2007).
19. D. Brassard, D. K. Sarkar, M. A. El Khakani and L. Ouellet, *J. Vac. Sci. Technol. A* **24**, 600 (2006).
20. D. Brassard, D. K. Sarkar, M. A. El Khakani and L. Ouellet, *J. Vac. Sci. Technol. A* **22**, 851 (2004).
21. D. K. Sarkar, X. J. Zhou, A. Tannous, M. Louie and K. T. Leung, *Solid State Commun.* **125**, 365 (2003).
22. D. K. Sarkar, X. J. Zhou, A. Tannous and K. T. Leung, *J. Phys. Chem. B (Letter)* **107**, 2879 (2003).
23. D. K. Sarkar, E. Desbiens and M. A. El Khakani, *Appl. Phys. Lett.* **80**, 294 (2002).
24. D. K. Sarkar, I. Rau, M. Falke, H. Giesler, S. Teichert, G. Beddies and H.-J. Hinneberg, *Appl. Phys. Lett.* **78**, 3604 (2001).
25. D. K. Sarkar, M. Falke, H. Giesler, S. Teichert, G. Beddies and H.-J. Hinneberg, *J. Appl. Phys.* **89**, 6506 (2001).
26. T. Sun, L. Feng, X. Gao and L. Jiang, *Acc. Chem. Res.* **38**, 644 (2005).
27. A. Lafuma and D. Quéré, *Nature Mater.* **2**, 457 (2003).

28. J. Li, J. Fu, Y. Cong, Y. Wu, L. J. Xue and Y. C. Han, *Appl. Surf. Sci.* **252**, 2229 (2006).
29. V. Stelmashuk, H. Biederman, D. Slavinska, J. Zemek and M. Trchova, *Vacuum* **77**, 131 (2005).
30. S. H. Kim, J. H. Kim, B. K. Kang and H. S. Uhm, *Langmuir* **21**, 12213 (2005).
31. D. Schondelmaier, S. Cramm, R. Klingeler, J. Morenzin, C. Zilkens and W. Eberhardt, *Langmuir*
18, 6242 (2002).
32. E. Honoso, S. Fujihara, I. Honma and H. Zhou, *J. Am. Chem. Soc.* **127**, 13458 (2005).
33. N. Saleema, D. K. Sarkar, M. Farzaneh and E. Sacher, in: *Proceedings of the 2006 NSTI Nanotechnology*
Conference and Trade Show, Boston, Massachusetts, USA, Vol. 3, p. 158 (2006).
34. H. Liu, L. Feng, J. Zhai, L. Jiang and D. B. Zhu, *Langmuir* **20**, 5659 (2004).
35. F. Shi, Z. Q. Wang and X. Zhang, *Adv. Mater.* **17**, 1005 (2005).
36. L. Jiang, Y. Zhao and J. Zhai, *Angew. Chem. Int. Ed.* **43**, 4338 (2004).
37. R. Menini and M. Farzaneh, *Polymer Intl* **57**, 77 (2008).
38. K. Acatay, E. Simsek, C. Ow-Yang and Y. Z.Menceloglu, *Angew. Chem. Int. Ed.* **43**, 5210 (2004).
39. O. Lev, M. Tsionsky, L. Rabinovich, V. Glezer, S. Sampath, I. Pancratov and J. Gun, *Anal. Chem.*
67, 22A (1995).
40. D. K. Sarkar and M. Farzaneh, *Appl. Surface Sci.* **254**, 3758 (2008).
41. D. K. Sarkar, M. Farzaneh and R. W. Paynter, *Mater. Letters* **62**, 1226 (2008).
42. A. Safaee, D. K. Sarkar and M. Farzaneh, *Appl. Surface Sci.* **254**, 2493 (2008).
43. N. Saleema and M. Farzaneh, *Appl. Surface Sci.* **254**, 2690 (2008).
44. S. A. Kulinich, M. Farzaneh and X. W. Du, *Inorganic Materials* **43**, 1067 (2007).
45. S. A. Kulinich and M. Farzaneh, *Vacuum* **79**, 255 (2005).
46. S. A. Kulinich and M. Farzaneh, *Surface Sci.* **573**, 379 (2004).
47. S. A. Kulinich and M. Farzaneh, *Appl. Surface Sci.* **230**, 232 (2004).
48. D. K. Sarkar and M. Farzaneh, in: *Contact Angle, Wettability and Adhesion*, K. L. Mittal (Ed.),
Vol. 5, pp. 271–278. VSP/Brill, Leiden (2008).
49. N. Saleema, D. K. Sarkar andM. Farzaneh, in: *Contact Angle,Wettability and Adhesion*, K. L. Mittal
(Ed.), Vol. 5, pp. 279–285. VSP/Brill, Leiden (2008).
50. A. Safaee, D. K. Sarkar andM. Farzaneh, in: *Contact Angle,Wettability and Adhesion*, K. L.Mittal
(Ed.), Vol. 5, pp. 287–293. VSP/Brill, Leiden (2008).
51. A. Safaee, D. K. Sarkar and M. Farzaneh, in: *Proceedings of the 2006 NSTI Nanotechnology*
Conference and Trade Show, Boston, Massachusetts, USA, Vol. 3, p. 190 (2006).
52. D. K. Sarkar and M. Farzaneh, in: *Proceedings of the 2006 NSTI Nanotechnology Conference and*
Trade Show, Boston, Massachusetts, USA, Vol. 3, p. 166 (2006).
53. J. M. Montero-Moreno, M. Sarret and C. Müller, *Surface Coatings Technol.* **201**, 6352 (2007).
54. V. Kapaklis, A. Georgiopoulos, P. Poulopoulos and C. Politis, *Physica E* **38**, 44 (2007).
55. C. Wang, Y. Song, J. Zhao and X. Xia, *Surf. Sci.* **600**, L38 (2006).
56. N. Garoff and S. Zauscher, *Langmuir* **18**, 6921 (2002).

57. A. Mills, S.-K. Lee, A. Lepre, I. P. Parkin and S. A. O'Neill, *Photochem. Photobiol. Sci.* **1**, 865
(2002).
58. V. K. Croutch and R. A. Hartley, *J. Coatings Technol.* **64**(815), 41 (1992).
59. B. Solmo and V. Gupta, *Mech. Mater.* **33**, 471 (2001).
60. D. N. Anderson and A. D. Reich, *NASA Technical Memorandum*, 107399 AIAAA-97-0303
(1997).
61. M. Javan-Mashmool, C. Volat and M. Farzaneh, *Hydrol. Process.* **20**, 645 (2006).